EES Batteries

PAPER

View Article Online
View Journal | View Issue

Cite this: *EES Batteries*, 2025, **1**, 1291

Synergistic 3D Ni/Pd air cathodes for optimizing the triple-phase boundary reaction and catalytic activity in Li–O_2 batteries†

Jiyeon Lim,‡[a] Seonyong Cho,‡[a] Gwangmin Bae,[a] Seonggon Han,[b] Joseph Harding,[b] Jong-woan Chung,[a] Gayea Hyun,[c] Yong-Mook Kang *[a] and Seokwoo Jeon *[a]

Li–O_2 batteries (LOBs) have attracted attention as promising next-generation energy storage devices for applications requiring high energy density due to their high theoretical energy density. The electrochemical performance of LOBs is determined by the reaction kinetics at the triple-phase boundary (TPB), where Li^+, e^-, and O_2 participate. However, conventional air cathodes face challenges such as the sluggish oxygen reduction reaction (ORR) and oxygen evolution reaction (OER), poor cycle life and reduced energy efficiency due to the limited TPB area, hindering their commercialization. To address these limitations, this study proposes a three-dimensional (3D) nanostructured Ni/Pd air cathode featuring highly ordered 3D Ni structures uniformly coated with Pd. Therein, 3D Ni forms a uniform TPB and serves as a current collector with excellent electrical conductivity and high mechanical strength. Additionally, Pd, uniformly deposited on the Ni surface, acts as a catalyst to enhance electrochemical reactions, while its spherical morphology increases surface roughness, thereby facilitating TPB expansion. The 3D Ni/Pd air cathode efficiently suppresses electrode oxidation, achieving the synergistic effects of uniform TPB formation and high catalytic activity of Pd. As a result, compared to the Ni foam/Pd air cathode with a limited TPB area, it exhibits a significant improvement in energy efficiency from 76.63% to 82.72% and cycle life from 33 to 136 cycles. This design emphasizes the synergistic integration of an ordered 3D topology and a Pd catalyst toward enhanced energy efficiency and chemical stability of LOBs.

Received 22nd April 2025,
Accepted 24th July 2025

DOI: 10.1039/d5eb00074b

rsc.li/EESBatteries

Broader context

As global awareness of environmental issues grows and eco-friendly technologies such as electric vehicles continue to advance, the demand for sustainable and high-energy-density energy storage systems is becoming increasingly critical. Lithium–oxygen batteries (LOBs) are considered some of the most promising alternatives to conventional lithium-ion batteries (LIBs) due to their exceptionally high theoretical energy density. However, their low reversibility and limited triple-phase boundary (TPB) formation result in poor cycling stability, hindering their practical application. In this study, we address the limitations of conventional electrodes by introducing a three-dimensional (3D) Ni/Pd cathode, in which spherical palladium particles are uniformly deposited on ordered 3D nickel structures with submicron-scale pores. This architecture enhances mass transport and facilitates the formation of uniform and abundant TPBs, thereby improving both energy efficiency and cycling performance. This work offers a promising strategy to overcome key limitations of LOBs through the synergistic effect of a well-engineered 3D architecture and strategic material selection, contributing to the realization of high-performance and sustainable energy storage systems.

Introduction

The rapid increase in energy demand has driven the development of Li-ion batteries (LIBs), which are now widely utilized as energy storage systems in diverse applications, including energy storage devices, electric vehicles and mobile devices.[1,2] However, LIBs have reached their theoretical energy density limits, necessitating the development of next-generation batteries for high-energy applications. To address these demands, Li–O_2 batteries (LOBs) have emerged as a promising alternative

[a]*Department of Materials Science and Engineering, Korea University, Seoul 02841, Republic of Korea. E-mail: jeon39@korea.ac.kr, dake1234@korea.ac.kr*
[b]*Department of Materials Science and Engineering, Korea Advanced Institute of Science and Technology (KAIST), Daejeon 34141, Republic of Korea*
[c]*Department of Nanoengineering, University of California San Diego, La Jolla, CA 92093, United States*

†Electronic supplementary information (ESI) available. See DOI: https://doi.org/10.1039/d5eb00074b

‡These authors contributed equally to this work.

due to their higher theoretical energy density (~3500 Wh kg^{-1}), compared to conventional LIBs.[3,4]

In LOBs, the discharge product Li_2O_2 is formed through the oxygen reduction reaction (ORR) at the triple-phase boundary (TPB), where O_2 from the air cathode, Li^+ from the liquid electrolyte, and e^- from the solid electrode meet. The electrochemical performance of LOBs is determined by the reaction kinetics involving these three reactants at the TPB. However, insoluble and insulating Li_2O_2 gradually accumulates non-uniformly on the electrode surface as cycling progresses.[5,6] This accumulation restricts the mass transport of reactants to the TPB, reducing discharge capacity and increasing overpotential during charging.[7–11] Such large overpotential promotes side reactions, notably the generation of reactive singlet oxygen ($^1O_2$),[12] a key contributor to electrolyte decomposition and cathode degradation.[13] Consequently, energy efficiency and cycling stability are significantly degraded.

To address these issues, G. Hyun *et al.* proposed a three-dimensional (3D) nanostructured Cu electrode, which facilitated homogeneous formation of TPBs within its continuously interconnected and spatially ordered architecture, enhancing reaction kinetics.[14] However, their study primarily focused on the impact of electrode structural engineering, without sufficient consideration of active materials, which are crucial for practical LOB performance. Given the importance of electrode stability in long-term operation, selecting a highly stable electrode material is essential. Noble metals (*e.g.*, Pt, Pd, Au, and Ru) offer excellent electrochemical catalytic activity and stability by modulating the adsorption properties of intermediates through their tunable d orbitals.[15] Notably, they contribute to reducing the overpotential during the charging process, thereby improving the energy efficiency of the battery. Despite these advantages, high cost remains a major barrier to commercialization. To overcome this limitation, material design of noble metal–transition metal hybrid catalysts has been explored as a viable alternative, delivering high performance at reduced cost.[16] Hybrid catalysts maximize efficiency by combining the catalytic activity and stability of noble metals with the structural reinforcement and cost reduction offered by transition metals.[17–23]

In this study, we propose a 3D Ni/Pd air cathode to promote uniform TPB formation and enhance chemical stability. The 3D continuous and ordered topology of Ni, with a pore size of 200–300 nm, exhibits high electrical conductivity and mechanical robustness, ensuring a homogeneous TPB throughout the air cathode and facilitating the uniform distribution of discharge products. Furthermore, uniformly dispersed Pd nanoparticles on the 3D Ni framework increase the surface roughness of the air cathode, thereby expanding the liquid/gas interface. This structural modification simultaneously provides high ORR/OER activity and accelerates the kinetics of the electrochemical reaction while reducing excessive use of noble metals. Consequently, the 3D Ni/Pd air cathode achieves a high initial energy efficiency of ~83% and maintains a stable cycle life of up to 136 cycles. It also effectively suppresses electrode oxidation and demonstrates excellent chemical stability. These findings highlight the synergetic effect between the ordered 3D porous topology and the catalytic activity of Pd in significantly improving both the electrochemical performance and long-term stability of LOBs.

Experimental

Fabrication of the freestanding 3D Ni/Pd film

A 3D porous polymeric template was fabricated on a conductive substrate using proximity-field nanopatterning (PnP). The detailed process of PnP is illustrated in ref. 24, 27, and 36. First, an SU-8 photoresist (Microchem) was spin-coated onto Ti/SiO_2 wafer (TASCO). After soft baking, a transparent phase mask, which has a square array of 600 nm periodicity, was conformally contacted on the photoresist exposed to collimated UV light using an Nd:YAG laser (wavelength 355 nm, Advanced Optowave Corp.). The periodic relief structure of the phase mask generated a 3D diffraction pattern in the proximity field and it was directly transcribed to the photoresist. The 3D polymeric template with 12 μm thickness was formed after the post-exposure baking and developing process. The 3D Ni nanostructures were obtained by an electroplating process. The fabricated 3D polymeric template was used as a working electrode, with a nickel plate serving as the counter electrode for electroplating in a two-electrode system. Commercial Ni plating solution (HanTech PMC) was used, and a pulse current of −9 mA with a 50% duty cycle was applied using a potentiostat (versaSTAT), resulting in approximately 8 μm thickness of the nickel layer. The 3D polymeric template was subsequently removed using a plasma etcher (STP compact, Muegge) to obtain the 3D Ni. The 3D Ni was then immersed in a 20% hydrofluoric acid (HF, 48%, Sigma) solution for 1 minute to create a freestanding 3D Ni structure. Electropolishing was performed to enlarge the pores of the 3D Ni structure. Pd was uniformly coated on the surface of the 3D Ni by electroplating with a three-electrode system. The Pd electroplating solution was prepared using 0.01 M $PdCl_2$ and 0.3 M HCl. The freestanding 3D Ni, an Ag/AgCl electrode (1 M KCl), and a Pt wire were used as the working electrode, reference electrode, and counter electrode, respectively. Pd deposition was carried out at a pulse voltage of −0.11 V with 9% duty cycle.

Assembling Li–O_2 cells

To fabricate the air cathode, 3D Ni/Pd was placed at the center of a carbon paper (CP) that had been preheated at 80 °C for 10 minutes. The CP was used as the gas diffusion layer. Then, 60 μL of Nafion binder, diluted 1 : 1 with IPA, was applied drop by drop to attach the sample to the CP. The fabricated 3D Ni/Pd air cathode was punched into a 12 mm diameter (approximately 1.1304 cm^2) air cathode for use in a Swagelok-type cell. The cell assembly was carried out in an inert atmosphere glove box, where lithium metal (anode), glass fiber (separator), 100 μL of electrolyte containing 1 M $LiCF_3SO_3$ in TEGDME (tetraethylene glycol dimethyl ether), and the 3D Ni/Pd air cathode were sequentially assembled. Afterward, the system

was purged with 99.999% O_2 gas for 5 minutes before performing electrochemical measurements.

Characterization

The morphology and elemental distribution of the fabricated 3D Ni/Pd air cathode were analyzed using field-emission scanning electron microscopy (FESEM, Quanta FEG 250, Thermo Fisher) and transmission electron microscopy (TEM, Talos F200X G2, Thermo Fisher) combined with energy-dispersive X-ray spectroscopy (EDS, Quanta FEG 250, Thermo Fisher). Characterization of chemical bonding and crystallographic analysis were conducted using X-ray photoelectron spectroscopy (XPS, Nexsa, Thermo Fisher) and X-ray diffraction (XRD, SmartLab, Rigaku), respectively. The contact angle in DI water and the electrolyte was measured using a pendant drop tensiometer (DSA100, KRUSS). The presence of discharge products was demonstrated using Raman spectroscopy (DXR2xi, Thermo) with 532 nm wavelength laser light.

Electrochemical measurements

The sheet resistance of the electrodes was measured using a four-point probe method (CMT-100S) at room temperature. The cell was tested under constant current measurements at a current density of 0.025 mA cm^{-2} within a voltage window of 2.0–4.5 V *vs.* Li/Li^+. Cyclic voltammetry (CV) measurements were performed at a scan rate of 0.05 mV s^{-1} within the same voltage range. Efficiency and cycle retention were compared through galvanostatic discharge/charge measurements, with the maximum capacity limited to 0.10 mAh cm^{-2}. Electrochemical impedance spectroscopy (EIS) spectra were recorded in the frequency range of 2 MHz–0.1 Hz with an AC voltage amplitude of 10.00 mV s^{-1} using an IviumStat workstation.

Results and discussion

Fabrication and characterization of 3D Ni/Pd cathodes

Fig. 1 presents a schematic diagram of an LOB, including the 3D Ni/Pd cathode. The 3D Ni/Pd structure consists of a periodic porous interconnected network with submicron-sized pores, which enhances mass transport by shortening the diffusion pathways for electrons and ions while expanding the reaction area through its large specific surface area. Additionally, this architecture enables the formation of uniform TPBs, thereby maximizing electrochemical performance. In contrast, the Ni foam/Pd structure features a non-periodic and irregular porous architecture, leading to a limited reaction area and uneven TPBs. These constrained TPBs hinder the interaction between Li^+, e^-, and O_2, significantly reducing mass transport efficiency.

Fig. 2a schematically illustrates the fabrication process of the 3D Ni/Pd nanostructure. An ordered porous 3D Ni structure was fabricated by first creating a 3D polymer template using proximity-field nanopatterning (PnP), an interference lithography technique.[24–30] This polymer template exhibits a body-centered tetragonal (BCT) arrangement, with a periodicity of 600 nm in the *x*–*y* direction and 1 μm in the *z* direction. The pores of the 3D polymer template were then filled with Ni using a pulsed electroplating process.[14,31–33] After removing the polymer template, the 3D Ni structure was detached from the substrate *via* hydrofluoric acid (HF) treatment. The free-standing 3D Ni structure has a thickness of approximately 8 μm and forms ordered submicron pores with a size of 200–300 nm (Fig. S1, ESI†). Subsequently, Pd particles were uniformly deposited on the surface of the 3D Ni structure using a pulsed electroplating method to produce the 3D Ni/Pd nanostructure. The fabricated 3D Ni/Pd structure was designed for stable support by attaching it to carbon paper, which functioned both as a gas diffusion layer and a structural backing layer. To achieve this, a 50% diluted Nafion solution was used as a binder, with the IPA-to-Nafion mixing ratio optimized in a previous study.[14]

Fig. 2b–d show the characterization results of the fabricated 3D Ni/Pd air cathode. The cross-sectional scanning electron microscopy (SEM) image shown in Fig. 2b confirms that Pd was uniformly deposited without blocking the pores of the 3D Ni structure. Energy-dispersive X-ray spectroscopy (EDS) mapping images match the SEM image, demonstrating that the Pd element is evenly distributed throughout the structure. This uniformity is maintained even at the nanoscale, as further evidenced by the transmission electron microscopy (TEM) image and EDS mapping shown in Fig. 2c. Fig. 2d presents the X-ray diffraction (XRD) pattern of the 3D Ni/Pd, with distinct diffraction peaks at 44.5°, 51.8° and 76.4°, corresponding to the (111), (200) and (220) planes of Ni, which is a face-centered cubic (FCC) structure. Additionally, peaks at 40.1°, 46.7° and 68.1° correspond to the (111), (200) and (220) planes of Pd, also exhibiting an FCC structure. The chemical composition of the fabricated 3D Ni/Pd was further confirmed through X-ray photoelectron spectroscopy (XPS) analysis (Fig. S2†).

Electrochemical analysis

To evaluate the effects of the Pd catalyst and structural differences, the electrochemical performance of the 3D Ni/Pd electrode was compared to that of 3D Ni, Ni foam/Pd, and Ni foam electrodes. Fig. 3a shows the first galvanostatic discharge–charge profile at a current density of 0.025 mA cm^{-2} with a capacity limit of 0.10 mAh cm^{-2}. During the charging process, each electrode exhibited different OER behaviors due to variations in discharge product decomposition efficiency.[34,35] As a result, the voltage hysteresis for the 3D Ni/Pd, 3D Ni, Ni foam/Pd and Ni foam electrodes were found to be 0.72 V, 1.49 V, 0.94 V, and 1.52 V at a capacity of 0.10 mAh cm^{-2}, respectively, based on the difference between the OER and ORR potentials at a capacity of 0.1 mAh. Notably, the 3D Ni/Pd electrode showed about a 50% reduction in voltage hysteresis compared to the 3D Ni electrode, which is attributed to the synergy between its ordered porous network and the high catalytic activity of Pd. To assess whether this reduction in overpotential stems from improved electronic conductivity or catalytic

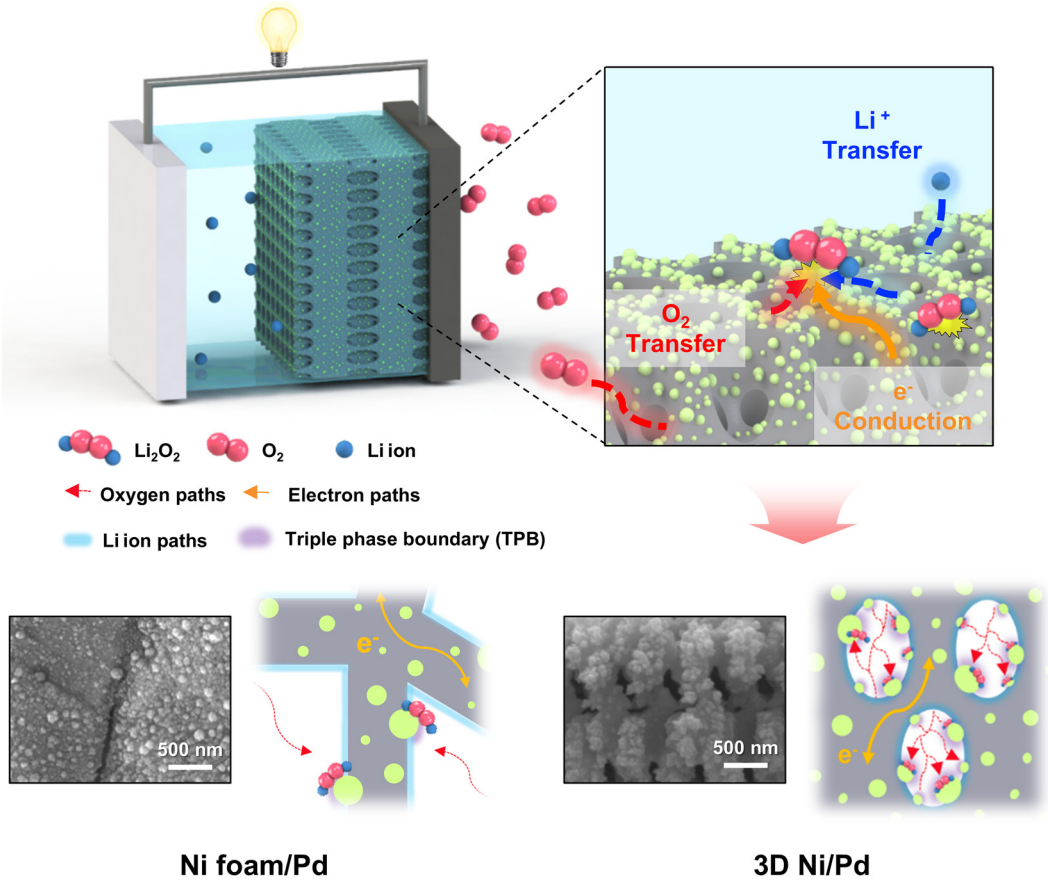

Fig. 1 Schematic illustration of the working principle of a Li–O_2 battery containing a 3D Ni/Pd air cathode.

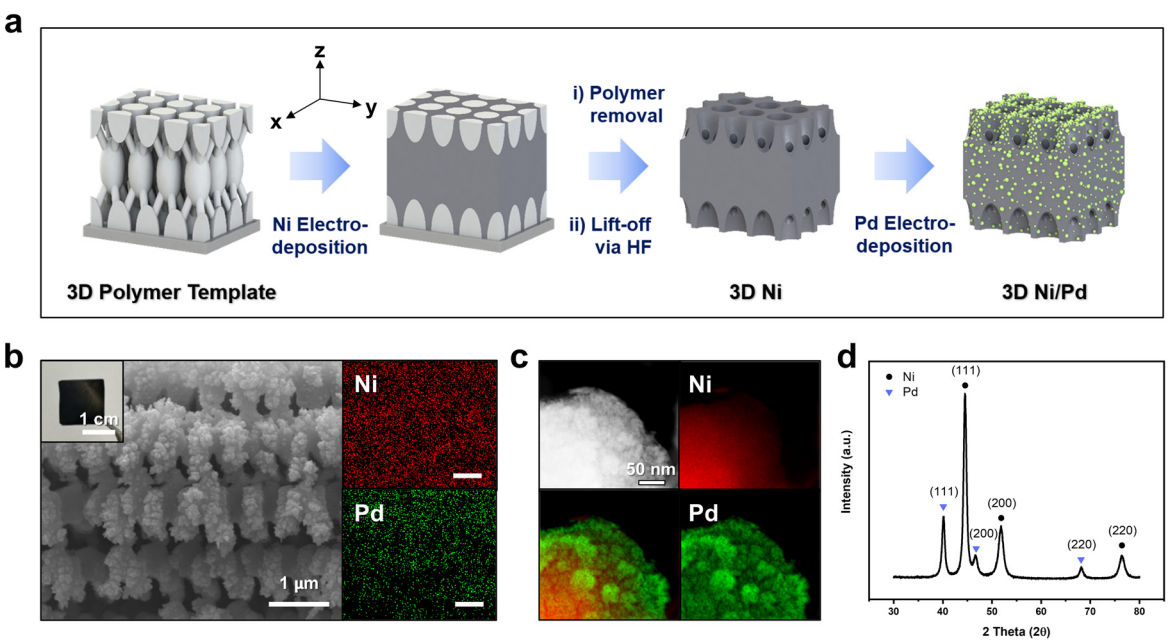

Fig. 2 Characterization of the 3D Ni/Pd air cathode. (a) Schematic illustration of the 3D Ni/Pd fabrication process. (b) Cross-sectional SEM and elemental mapping images of 3D Ni/Pd (inset: digital image of the 3D Ni/Pd film). (c) TEM and elemental mapping images of 3D Ni/Pd. (d) XRD pattern confirming the formation of the Ni/Pd structure.

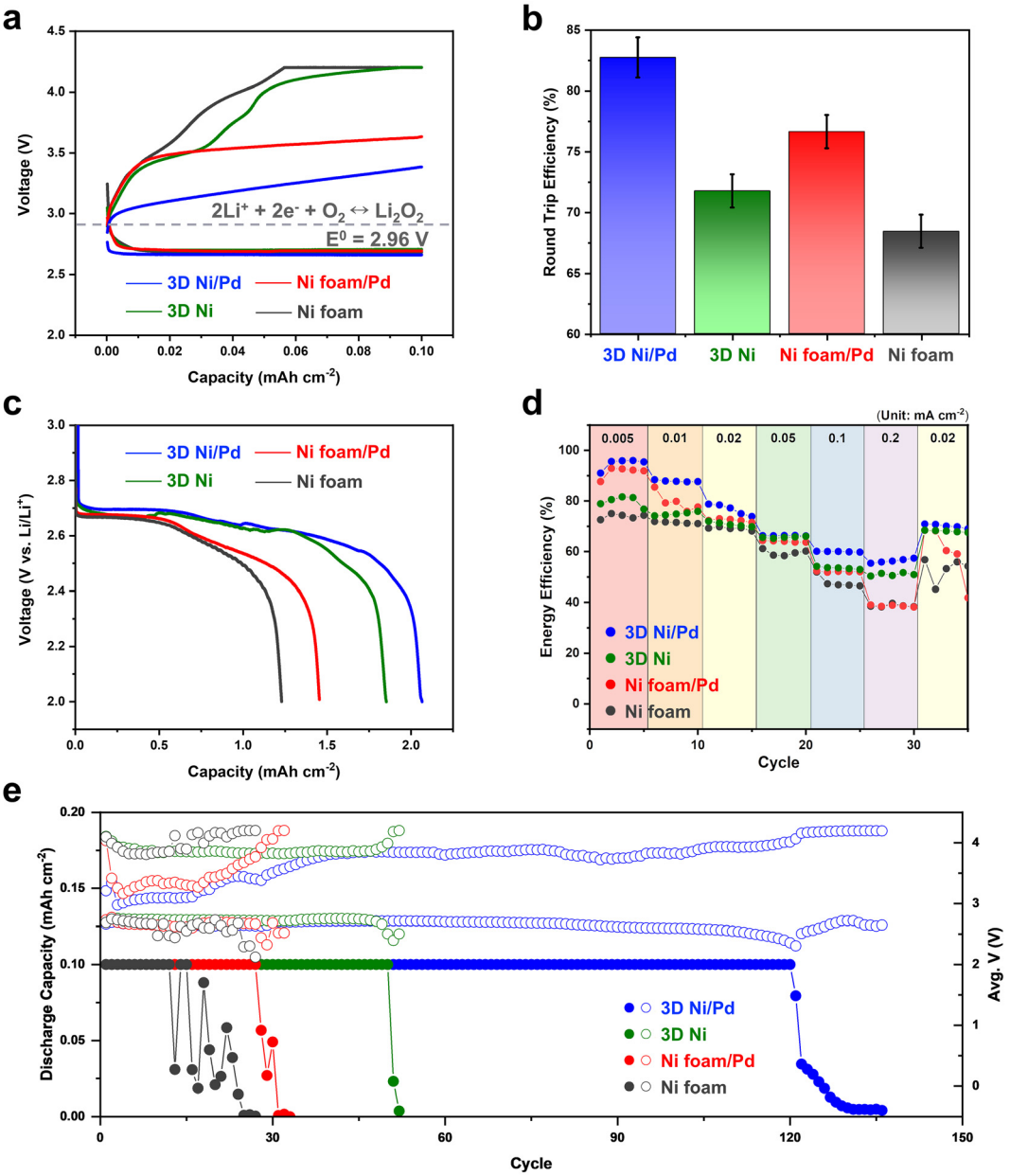

Fig. 3 Electrochemical analysis. (a) First galvanostatic discharge–charge curves of each electrode and (b) round trip efficiency. (c) Discharge profiles of the first cycle at a current density of 0.025 mA cm^{-2} and (d) energy efficiency profiles of Li–O_2 cells under various current density conditions with a limited capacity of 0.1 mAh cm^{-2}. (e) Cycle retention and average voltage variation within a limited capacity up to 0.10 mAh cm^{-2} at a current density of 0.02 mA cm^{-2}.

effects, the resistivity of each electrode was evaluated based on the measured sheet resistance and thickness (Table S1†). The 3D Ni electrode has lower resistivity (6.79×10^{-5} Ω cm) than Ni foam (1.01×10^{-4} Ω cm), which is attributed to its interconnected framework that supports more efficient electron transport. Upon Pd incorporation, the resistivity decreased further to 4.27×10^{-5} Ω cm for the 3D Ni/Pd and 5.83×10^{-5} Ω cm for the Ni foam/Pd electrode. However, although the resistivity values of 3D Ni/Pd, 3D Ni, and Ni foam/Pd are comparable, their voltage hysteresis shows a marked difference. This discrepancy suggests that electronic conductivity alone cannot account for the observed performance variations. Rather, the pronounced improvement in the 3D Ni/Pd electrode highlights the synergistic role of Pd catalytic activity at the TPB. Meanwhile, both the 3D Ni and Ni foam electrodes exhibited similar voltage hysteresis, primarily due to the intrinsic catalytic activity of metallic Ni. Due to the reduced overpotential, the 3D Ni/Pd electrode achieved the highest energy efficiency of 82.72%. In comparison, the efficiencies of the 3D Ni, Ni foam/Pd and Ni foam electrodes were 71.74%, 76.63% and

68.41%, following the trend of voltage hysteresis results (Fig. 3b). This improvement in energy efficiency suggests that discharge products decompose more efficiently during the charging process.[35,36]

As shown in Fig. 3c, the maximum discharge capacity of each electrode was compared by discharging at a current density of 0.025 mA cm^{-2} until reaching 2.00 V *vs.* Li/Li^+. The discharge capacity is determined by the amount of Li_2O_2 formed at the TPB, so the characteristics of the TPB significantly impact the discharge capacity. Although differences in the actual surface area may contribute to electrochemical performance, the structural design of the electrode appears to be a more decisive factor. Hyun *et al.* reported that a 3D nanostructured Cu electrode with a lower Brunauer–Emmett–Teller (BET) surface area (0.0249 m^2 g^{-1}) outperformed Cu foam (0.4216 m^2 g^{-1}) in electrochemical performance.[14] Given the identical structural features and pore sizes of the 3D Ni-based (200–300 nm) and Ni foam-based (100–300 μm) electrodes used in this study, these values provide a reasonable reference for comparison. Based on this comparison, the lower electrochemical performance of the Cu foam despite its larger surface area suggests that the enhanced performance observed in this study is primarily attributed to the formation of TPB and optimization of reaction pathways through structural design rather than surface area differences alone. To evaluate wettability, which correlates with the density of TPB, contact angle measurements with DI water and electrolyte (Table S2†) were conducted.[1,37] The 3D Ni/Pd electrode shows a contact angle of 114.56° ± 4.66° with DI water while the 3D Ni electrode shows 103° ± 2.88°, reflecting its enhanced hydrophobicity. This improvement is associated with the Pd decorated surface, which increases the surface roughness of the electrode. According to the Cassie–Baxter model, the resulting surface morphology leads to the formation of larger air pockets beneath the droplet and an increased liquid/gas interface.[38,39] Consequently, the increased surface roughness resulting from Pd decoration promotes the formation of an extended TPB. Despite the inherently good wettability of TEGDME, the 3D Ni/Pd electrode still showed the largest contact angle of 62.13° ± 3.49°, further confirming an increased gas phase ratio in TPB. Since O_2 diffusivity is significantly higher in the gas phase than in liquid,[40] this implies that the 3D Ni/Pd electrode facilitates faster O_2 transport compared to other electrodes. Consequently, with its abundant and homogeneous TPB and enhanced O_2 transport properties, the 3D Ni/Pd electrode exhibited the highest discharge capacity of 2.07 mAh cm^{-2}.

In contrast, the Ni foam/Pd electrode exhibited high wettability with a contact angle of 52.34° ± 2.47°. This high wettability causes excessive electrolyte infiltration during battery operation, limiting the mass transport of gaseous O_2 and reducing its availability at the reaction interface, thereby restricting TPB formation.[37,41] As a result, the Ni foam/Pd electrode showed a reduced discharge capacity of 1.45 mAh cm^{-2}. Additionally, when the discharge capacity reached approximately 0.7 mAh cm^{-2}, the voltage curve began to bend and hysteresis increased. This behavior suggests insufficient TPB and poor O_2 diffusion in foam-based electrodes. These mass transport differences, arising from the electrode structure, were further corroborated by electrochemical impedance spectroscopy (EIS) analysis, as shown in Fig. S3.† In the Warburg region of both the open-circuit and discharged states (0.50 mAh cm^{-2}), the 3D Ni-based electrode exhibited a steeper slope than the foam-based electrode, indicating superior diffusion characteristics.[42,43] In the open-circuit state, the 3D Ni-based electrode exhibited a single semicircle, whereas the foam-based electrode exhibited two distinct semicircles. The appearance of a single semicircle in the 3D Ni electrode can be attributed to its ordered and interconnected topology, which promotes uniform electron transport and ensures conformal contact with the carbon paper, thereby enabling consistent and efficient charge transfer through a unified interface. In contrast, the two semicircles observed in the foam-based electrode indicate multiple interfacial resistances, due to its irregular structure and poor contact with the carbon paper, resulting in non-uniform charge transport. After discharge, however, the foam-based electrode also exhibited a single semicircle, which suggests that the interfacial process became less distinguishable in the impedance response, due to the formation of Li_2O_2.[44] In the charge transfer region of the discharged state, the 3D Ni-based electrode exhibited a smaller semicircle than the Ni foam-based electrode, indicating improved charge transfer and reduced resistance associated with Li_2O_2 formation and side reactions.[45,46] These results demonstrate that the homogeneous and abundant TPBs, coupled with enhanced O_2 diffusivity within the 3D Ni-based electrode, contribute to more efficient Li_2O_2 formation and greater discharge capacity.

The improved O_2 transport characteristics of the 3D Ni-based electrode are further reflected in its rate-dependent performance, as shown in Fig. 3d. At low current densities (0.005 and 0.01 mA cm^{-2}), Pd-containing electrodes exhibit higher energy efficiency, which is attributed to the catalytic promotion of Li_2O_2 decomposition. In contrast, at higher current densities where oxygen diffusion into the pore network becomes the rate-limiting step,[47,48] the 3D Ni-based electrodes show higher energy efficiency than the foam-based electrodes due to their interconnected porous architecture and greater volume of gas-phase within the TPB, which together enhance mass transport. Fig. S4† shows the cyclic voltammetry (CV) curves of different electrodes. The 3D Ni/Pd electrode, with abundant TPBs, displayed the largest CV curve area, indicating improved reaction kinetics for the ORR.[49] In contrast, the Ni foam electrode exhibited the smallest curve area. Although the Ni foam/Pd electrode contained the Pd catalyst, its reaction kinetics were not significantly enhanced, whereas the addition of Pd to the 3D Ni structure resulted in a more substantial improvement. Building on this knowledge, the cycle retention and average voltage variation for each electrode were evaluated under a current density of 0.02 mA cm^{-2} with a limited capacity of 0.10 mAh cm^{-2} (Fig. 3e). The 3D Ni/Pd electrode demonstrated excellent capacity retention up to the 136th

cycle, along with a minimal overpotential during the initial stage. The high energy efficiency and long cycle life of the 3D Ni/Pd electrode are attributed to its homogeneous and abundant TPB with a uniform distribution of the Pd catalyst, resulting in uniform formation and facile decomposition of discharge products. Notably, despite signs of degradation in the 120th cycle, the average voltage variation remained stable, indicating that reaction nonuniformity within the electrode was effectively suppressed. The 3D Ni electrode maintained a stable average voltage and discharge capacity up to the 52nd cycle outperforming the Ni foam and Ni foam/Pd electrodes. However, due to the absence of the Pd catalyst, the discharge products were not efficiently decomposed and accumulated on the electrode, deteriorating the overpotential and energy efficiency. The Ni foam/Pd electrode maintained its capacity up to the 33rd cycle, exhibiting a lower initial overpotential, which suggests that the addition of Pd improved Li_2O_2 decomposition efficiency. Despite the reduction in the initial overpotential, the Pd incorporation did not significantly improve the cycle life compared to the Ni foam electrode. This limitation stems from the structural constraints of the foam-based electrode, where the formation of TPB is restricted, resulting in a highly concentrated reaction interface. As a result, Pd utilization becomes uneven, and localized electrochemical stress accelerates its degradation, ultimately limiting its long-term catalytic effectiveness.

The 3D topology provides a homogeneous TPB, ensuring a more uniform reaction interface. This promotes the even dispersion of Pd across the electrode, effectively mitigating localized electrochemical stress and delaying degradation.[14,49] Through the incorporation of Pd, the 3D Ni/Pd electrode achieved superior electrochemical stability and enhanced capacity compared to other electrodes.

Chemical stability analysis

To examine the structural effects on electrode stability, X-ray photoelectron spectroscopy (XPS) and SEM analyses were performed. Fig. 4a and b present the top-view and cross-sectional SEM images of the degraded 3D Ni/Pd and Ni foam/Pd electrodes, while Fig. S5a and S5b† show the corresponding images of the degraded 3D Ni and Ni foam electrodes. While both electrodes were covered with discharge products, the foam-based electrode exhibited structural damage, whereas the 3D-based electrode maintained its structural integrity, demonstrating superior stability.

Fig. 4c and d show the comparison of the oxidation states of Ni and Pd in the pristine and degraded 3D Ni/Pd and Ni foam/Pd electrodes based on Ni 2p and Pd 3d XPS spectra. In the degraded 3D Ni/Pd electrode, the uniformly distributed Pd effectively mitigated Ni oxidation, as evidenced by the minimal shift in the Ni 2p peak compared to the 3D Ni electrode (Fig. S5c†). In contrast, the Ni foam/Pd electrode exhibited a pronounced Ni 2p peak shift to a lower binding energy, similar to the Ni foam (Fig. S5d†), indicating severe Ni oxidation.

Additionally, in the degraded 3D Ni/Pd electrode, the Pd peak exhibited only a slight shift, suggesting its resistance to oxidation. However, the Ni foam/Pd electrode displayed a significant Pd peak shift, reflecting extensive oxidation and degradation. This disparity in Pd stability is attributed to the inhomogeneous TPB of the Ni foam structure, where Pd accumulated in localized regions, leading to excessive electrochemical stress and ultimately making the catalyst unsuitable for long-term operation. Conversely, in the 3D Ni/Pd electrode, Pd was evenly dispersed, ensuring a well-distributed TPB that minimized electrochemical stress, thereby enhancing the stability of both the catalyst and the electrode.

The oxidation behavior of Ni and Pd is closely linked to the spatial distribution and decomposition characteristics of Li_2O_2. In the 3D Ni/Pd electrode, the homogeneous TPB promotes uniform Li_2O_2 nucleation, resulting in a thin-film morphology. *Ex situ* XRD and Raman analyses of the discharged 3D Ni/Pd electrode confirm that the primary discharge product is Li_2O_2, as indicated by characteristic diffraction peaks at 32.98°, 34.97°, and 58.72°, along with the O–O stretching vibration at 788 cm^{-1} in the Raman spectrum (Fig. S6†).[50,51] This thin-film Li_2O_2 is not only readily decomposed during charging, lowering the overpotential, but also beneficial for alleviating electrochemical and mechanical stress at the reaction interface (Fig. S7a and S7b†).[11,52,53] The constrained TPB in the Ni foam/Pd electrode leads to localized Li_2O_2 nucleation and growth, forming bulk toroidal-shaped Li_2O_2 deposits (Fig. S7c†). These bulk Li_2O_2 deposits contribute to high overpotential and exacerbate electrochemical and mechanical stress, which accelerate the oxidation of the catalyst and electrode degradation.[53,54] Thus, the 3D Ni/Pd electrode effectively mitigates surface oxidation and sustains high electrochemical performance through the synergistic effect of its ordered 3D porous structure and uniform Pd distribution. The Ni foam/Pd electrode, with its uneven Pd distribution, experiences rapid degradation, leading to poor cycling stability.

The degradation of the catalyst accelerates side reactions, which in turn negatively impacts the long-term stability of the electrode. To elucidate this effect, Li 1s and O 1s XPS analyses were conducted to examine the composition of ideal discharge products (Li_2O_2) and side reaction products (Li_2CO_3, LiOH) (Fig. 5). The results revealed a predominant presence of side reaction products, particularly Li_2CO_3, on the Ni foam/Pd electrode, indicating severe catalyst degradation and parasitic reactions. This degradation is attributed to the restricted TPB formation caused by a disordered porous structure with a non-uniform catalyst distribution. Furthermore, the constrained pore structure of the foam-based electrode impedes gaseous O_2 transport, leading to localized reaction at the TPB. Consequently, Li_2O_2 formation becomes highly concentrated in specific regions, exacerbating electrochemical stress and promoting unwanted side reactions. The accumulation of these byproducts not only reduces Li_2O_2 decomposition efficiency but also elevates the overpotential during charging, accelerating electrode degradation.[55,56]

In the 3D Ni/Pd electrode, Li_2O_2 formation was dominant, while Li_2CO_3 and LiOH signals remained relatively low, indi-

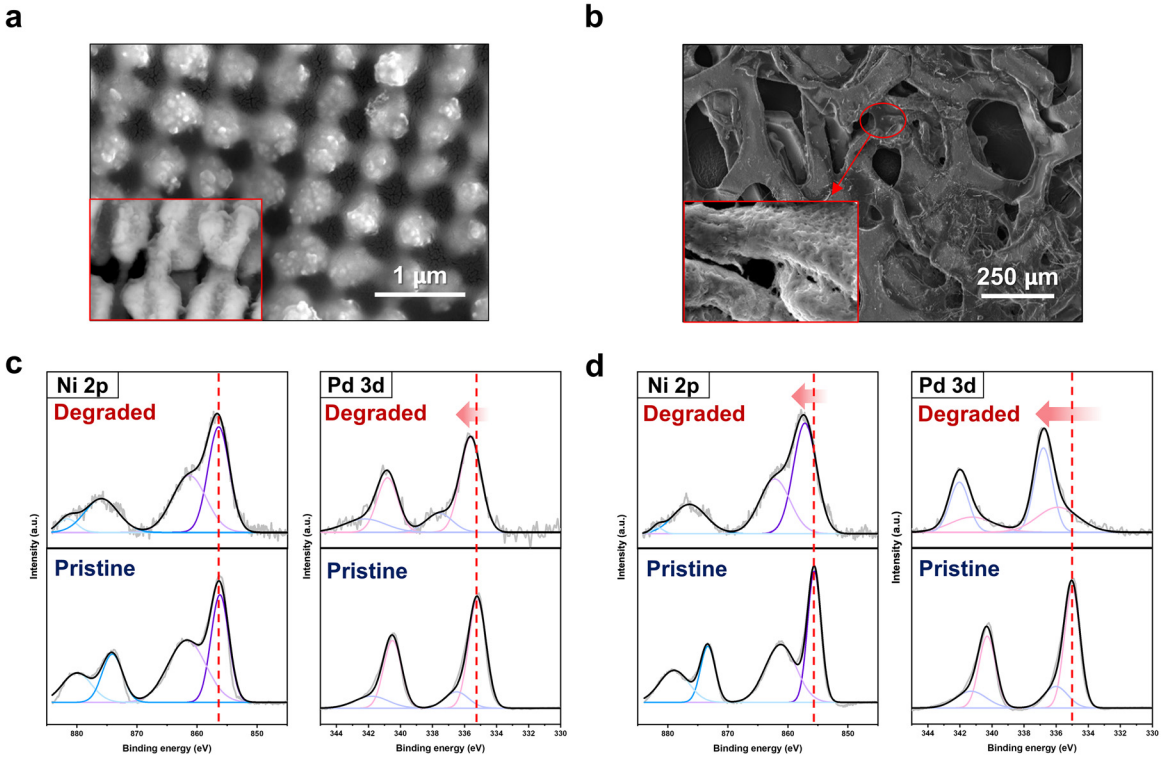

Fig. 4 SEM images after performance degradation of (a) 3D Ni/Pd and (b) Ni foam/Pd. Ni 2p and Pd 3d XPS spectra of (c) 3D Ni/Pd and (d) Ni foam/Pd.

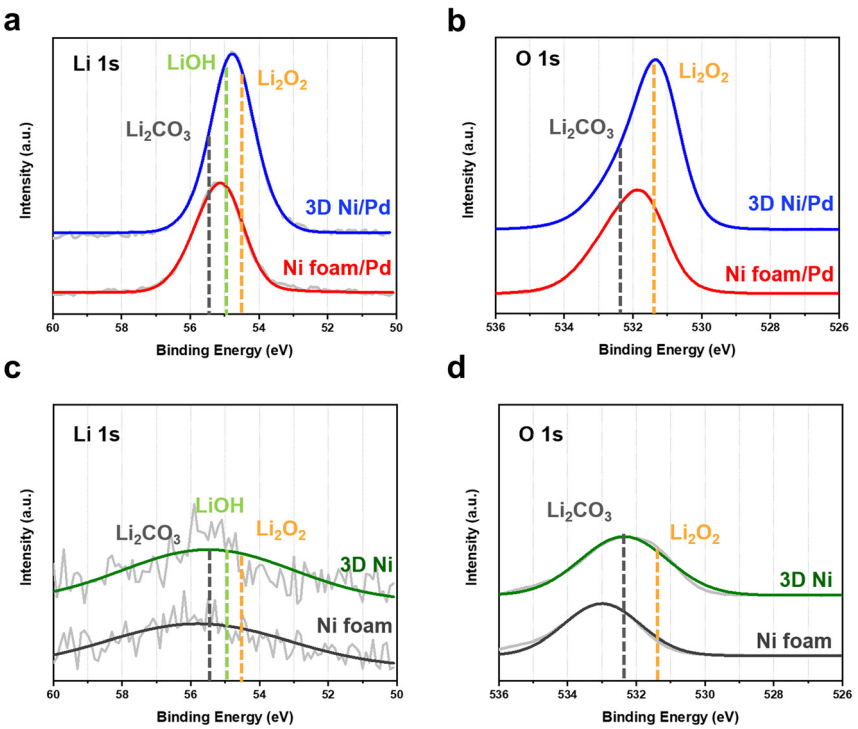

Fig. 5 XPS spectra of Li 1s and O 1s for degraded electrodes: Comparison of discharge products and side reactions for 3D Ni and Ni foam (a and b) with and (c and d) without Pd coating.

cating minimal side reaction product formation. These findings underscore the critical role of the synergy between an ordered 3D porous structure and homogeneous Pd catalyst dispersion in stabilizing electrochemical reactions. The spherical morphology of Pd enhances catalytic activity while simultaneously modifying the electrode surface in a way that promotes TPB expansion. By ensuring homogeneous TPB formation, efficient O_2 transport, and catalyst stability, the 3D Ni/Pd electrode minimizes side reactions and improves long-term battery performance.

Conclusions

In conclusion, we demonstrated a highly ordered 3D porous Ni/Pd air cathode using PnP and electroplating techniques. Compared to other cathode designs, including 3D Ni, Ni foam, and Ni foam/Pd, the 3D Ni/Pd air cathode exhibited the highest electrochemical activity and stability, achieving a low overpotential of 0.72 V, a high energy efficiency of 82.72%, and a cycle life up to 136 cycles. This exceptional performance was attributed to the formation of homogeneous and extended TPBs within the 3D topology, which facilitated efficient electrochemical reactions. XPS analysis further confirmed that the 3D Ni/Pd air cathode suppressed Pd and Ni oxidation, preserving catalyst integrity and enhancing the long-term stability. These findings highlight the synergistic effect of a well-engineered 3D architecture and strategic material selection in improving the electrochemical performance and durability of LOBs.

Author contributions

G. Hyun, Y.-M. Kang, and S. Jeon designed and conceived the experiments. J. Lim fabricated the 3D Ni/Pd air cathode and conducted SEM, XRD, XPS, and contact angle measurements. S. Cho and J.-W. Chung conducted the electrochemical measurements. S. Han designed the electroplating conditions for Pd. J. Harding conducted the TEM analysis. G. Bae commented on the manuscript. All authors discussed and analyzed the results.

Conflicts of interest

There are no conflicts of interest to declare.

Data availability

The data supporting this article have been included as part of the ESI.†

Acknowledgements

This research was supported by the Creative Materials Discovery Program through the National Research Foundation of Korea (NRF) funded by the Korean Government (MSIT) [grant numbers NRF-2020M3D1A1110522 and NRF-2020M3D1A1110527]. It was also supported by the NRF grant funded by MSIT [grant numbers NRF-2022M3H4A1A04068923 and RS-2025-00553909].

References

1 S. Cho, H. Jung, M. Park, L. Lyu and Y.-M. Kang, *ACS Energy Lett.*, 2024, **9**, 2848–2857.
2 F. Degen, M. Winter, D. Bendig and J. Tübke, *Nat. Energy*, 2023, **8**, 1284–1295.
3 W.-J. Kwak, A. Rosy, D. Sharon, C. Xia, H. Kim, L. R. Johnson, P. G. Bruce, L. F. Nazar, Y.-K. Sun and A. A. Frimer, *Chem. Rev.*, 2020, **120**, 6626–6683.
4 Z. Ma, X. Yuan, L. Li, Z.-F. Ma, D. P. Wilkinson, L. Zhang and J. Zhang, *Energy Environ. Sci.*, 2015, **8**, 2144–2198.
5 T. K. Zakharchenko, A. V. Sergeev, A. D. Bashkirov, P. Neklyudova, A. Cervellino, D. M. Itkis and L. V. Yashina, *Nanoscale*, 2020, **12**, 4591–4601.
6 S. Ding, X. Yu, Z.-F. Ma and X. Yuan, *J. Mater. Chem. A*, 2021, **9**, 8160–8194.
7 A. Dunst, V. Epp, I. Hanzu, S. A. Freunberger and M. Wilkening, *Energy Environ. Sci.*, 2014, **7**, 2739–2752.
8 O. Gerbig, R. Merkle and J. Maier, *Adv. Mater.*, 2013, **25**, 3129–3133.
9 S. Lau and L. A. Archer, *Nano Lett.*, 2015, **15**, 5995–6002.
10 S. Yang, P. He and H. Zhou, *Energy Storage Mater.*, 2018, **13**, 29–48.
11 Y. Zhang, Q. Cui, X. Zhang, W. C. McKee, Y. Xu, S. Ling, H. Li, G. Zhong, Y. Yang and Z. Peng, *Angew. Chem.*, 2016, **128**, 10875–10879.
12 J. Wandt, P. Jakes, J. Granwehr, H. A. Gasteiger and R. A. Eichel, *Angew. Chem., Int. Ed.*, 2016, **55**, 6892–6895.
13 N. Mahne, B. Schafzahl, C. Leypold, M. Leypold, S. Grumm, A. Leitgeb, G. A. Strohmeier, M. Wilkening, O. Fontaine and D. Kramer, *Nat. Energy*, 2017, **2**, 1–9.
14 G. Hyun, M. Park, G. Bae, J. w. Chung, Y. Ham, S. Cho, S. Jung, S. Kim, Y. M. Lee and Y. M. Kang, *Adv. Funct. Mater.*, 2023, **33**, 2303059.
15 Y. Zhou and S. Guo, *eScience*, 2023, **3**, 100123.
16 Z.-L. Jiang, J. Xie, C.-S. Luo, M.-Y. Gao, H.-L. Guo, M.-H. Wei, H.-J. Zhou and H. Sun, *RSC Adv.*, 2018, **8**, 23397–23403.
17 Z. Bai, X. Chen and C. Liang, *Ind. Eng. Chem. Res.*, 2023, **62**, 6069–6080.
18 G. Bampos, S. Bebelis, D. I. Kondarides and X. Verykios, *Top. Catal.*, 2017, **60**, 1260–1273.
19 R. Choi, J. Jung, G. Kim, K. Song, Y.-I. Kim, S. C. Jung, Y.-K. Han, H. Song and Y.-M. Kang, *Energy Environ. Sci.*, 2014, **7**, 1362–1368.

20 O. g. G. Ellert, M. V. Tsodikov, S. A. Nikolaev and V. M. Novotortsev, *Russ. Chem. Rev.*, 2014, **83**, 718.
21 K. A. Goulas, S. Sreekumar, Y. Song, P. Kharidehal, G. Gunbas, P. J. Dietrich, G. R. Johnson, Y. Wang, A. M. Grippo and L. C. Grabow, *J. Am. Chem. Soc.*, 2016, **138**, 6805–6812.
22 A. K. Singh and Q. Xu, *ChemCatChem*, 2013, **5**, 652–676.
23 K. Zhao, Y. Shu, F. Li and G. Peng, *Green Energy Environ.*, 2023, **8**, 1043–1070.
24 C. Ahn, J. Park, D. Cho, G. Hyun, Y. Ham, K. Kim, S.-H. Nam, G. Bae, K. Lee and Y.-S. Shim, *Funct. Compos. Struct.*, 2019, **1**, 032002.
25 J. K. Hyun, J. Park, E. Kim, L. J. Lauhon and S. Jeon, *Adv. Opt. Mater.*, 2014, **2**, 1213–1220.
26 S. Jeon, J.-U. Park, R. Cirelli, S. Yang, C. E. Heitzman, P. V. Braun, P. J. Kenis and J. A. Rogers, *Proc. Natl. Acad. Sci. U. S. A.*, 2004, **101**, 12428–12433.
27 C. Lee, G. Chang, J. Kim, G. Hyun, G. Bae, S. So, J. Yun, J. Seong, Y. Yang and D. Y. Park, *ACS Photonics*, 2022, **10**, 919–927.
28 S.-H. Nam, M. Kim, N. Kim, D. Cho, M. Choi, J. H. Park, J. Shin and S. Jeon, *Sci. Adv.*, 2022, **8**, eabm6310.
29 J. Park, J. H. Park, E. Kim, C. W. Ahn, H. I. Jang, J. A. Rogers and S. Jeon, *Adv. Mater.*, 2011, **23**, 860.
30 J. Park, D. Tahk, C. Ahn, S. G. Im, S.-J. Choi, K.-Y. Suh and S. Jeon, *J. Mater. Chem. C*, 2014, **2**, 2316–2322.
31 Y. Ham, N. J. Fritz, G. Hyun, Y. B. Lee, J. S. Nam, I.-D. Kim, P. V. Braun and S. Jeon, *Energy Environ. Sci.*, 2021, **14**, 5894–5902.
32 G. Hyun, S. Cao, Y. Ham, D.-Y. Youn, I.-D. Kim, X. Chen and S. Jeon, *ACS Nano*, 2022, **16**, 9762–9771.
33 G. Hyun, J. T. Song, C. Ahn, Y. Ham, D. Cho, J. Oh and S. Jeon, *Proc. Natl. Acad. Sci. U. S. A.*, 2020, **117**, 5680–5685.
34 S. Kang, Y. Mo, S. P. Ong and G. Ceder, *Chem. Mater.*, 2013, **25**, 3328–3336.
35 H.-D. Lim, B. Lee, Y. Bae, H. Park, Y. Ko, H. Kim, J. Kim and K. Kang, *Chem. Soc. Rev.*, 2017, **46**, 2873–2888.
36 K. Song, D. A. Agyeman, M. Park, J. Yang and Y. M. Kang, *Adv. Mater.*, 2017, **29**, 1606572.
37 F. Wang and X. Li, *ACS Omega*, 2018, **3**, 6006–6012.
38 P. Forsberg, F. Nikolajeff and M. Karlsson, *Soft Matter*, 2011, **7**, 104–109.
39 C. Lee and C.-J. Kim, *Phys. Rev. Lett.*, 2011, **106**, 014502.
40 I. M. Krieger, G. W. Mulholland and C. S. Dickey, *J. Phys. Chem.*, 1967, **71**, 1123–1129.
41 H. Song, S. Xu, Y. Li, J. Dai, A. Gong, M. Zhu, C. Zhu, C. Chen, Y. Chen and Y. Yao, *Adv. Energy Mater.*, 2018, **8**, 1701203.
42 I. Bardenhagen, O. Yezerska, M. Augustin, D. Fenske, A. Wittstock and M. Bäumer, *J. Power Sources*, 2015, **278**, 255–264.
43 J. Huang, *Electrochim. Acta*, 2018, **281**, 170–188.
44 H. Arai, S. Müller and O. Haas, *J. Electrochem. Soc.*, 2000, **147**, 3584.
45 J. Højberg, B. D. McCloskey, J. Hjelm, T. Vegge, K. Johansen, P. Norby and A. C. Luntz, *ACS Appl. Mater. Interfaces*, 2015, **7**, 4039–4047.
46 I. Landa-Medrano, I. R. de Larramendi, N. Ortiz-Vitoriano, R. Pinedo, J. I. R. de Larramendi and T. Rojo, *J. Power Sources*, 2014, **249**, 110–117.
47 Z. Su, V. De Andrade, S. Cretu, Y. Yin, M. J. Wojcik, A. A. Franco and A. Demortière, *ACS Appl. Energy Mater.*, 2020, **3**, 4093–4102.
48 J. Liu, S. K. Rahimian and C. W. Monroe, *Phys. Chem. Chem. Phys.*, 2016, **18**, 22840–22851.
49 B. D. McCloskey, R. Scheffler, A. Speidel, G. Girishkumar and A. C. Luntz, *J. Phys. Chem. C*, 2012, **116**, 23897–23905.
50 F. S. Gittleson, K. P. Yao, D. G. Kwabi, S. Y. Sayed, W. H. Ryu, Y. Shao-Horn and A. D. Taylor, *ChemElectroChem*, 2015, **2**, 1446–1457.
51 C. Song, K. Ito, O. Sakata and Y. Kubo, *RSC Adv.*, 2018, **8**, 26293–26299.
52 B. D. Adams, C. Radtke, R. Black, M. L. Trudeau, K. Zaghib and L. F. Nazar, *Energy Environ. Sci.*, 2013, **6**, 1772–1778.
53 B. M. Gallant, D. G. Kwabi, R. R. Mitchell, J. Zhou, C. V. Thompson and Y. Shao-Horn, *Energy Environ. Sci.*, 2013, **6**, 2518–2528.
54 M. Park, S. Cho, J. Yang, V. W.-h. Lau, K. H. Kim, J. H. Park, S. Ringe and Y.-M. Kang, *J. Am. Chem. Soc.*, 2023, **145**, 15425–15434.
55 Z. Zhao, J. Huang and Z. Peng, *Angew. Chem., Int. Ed.*, 2018, **57**, 3874–3886.
56 B. D. McCloskey, A. Speidel, R. Scheffler, D. Miller, V. Viswanathan, J. Hummelshøj, J. Nørskov and A. Luntz, *J. Phys. Chem. Lett.*, 2012, **3**, 997–1001.